Geophys. J. Int. (2003) **154,** 811–828

Source mechanisms of deep and intermediate-depth low-frequency earthquakes beneath Iwate volcano, northeastern Japan

Haruhisa Nakamichi,* Hiroyuki Hamaguchi, Satoru Tanaka, Sadato Ueki, Takeshi Nishimura and Akira Hasegawa

Research Center for Prediction of Earthquakes and Volcanic Eruptions, Graduate School of Science, Tohoku University, Sendai 980-8578, *Japan*

Accepted 2003 March 24. Received 2003 March 18; in original form 2001 December 17

SUMMARY

The 1998–1999 volcanic unrest of Iwate volcano, northeastern Japan, was marked by 350 deep low-frequency earthquakes (DLFs) and 120 intermediate-depth low-frequency earthquakes (ILFs), as well as an intense swarm of shallow volcanic earthquakes that began during 1998 April. The rate of occurrence of the DLFs increased approximately 5 d before that of the shallow volcanic earthquakes increased, and the number of ILFs gradually increased from the middle of 1998. To investigate the relationship between the shallow volcanic activity and the activities of the DLFs and ILFs, we determined their precise hypocentres and source mechanisms by analysing waveform data recorded by a dense seismic network of 47 three-component seismometers located on and around the volcano. The hypocentres of DLFs are concentrated within three regions: the first region is at depths from 31 to 34 km, approximately 10 km south of the summit, the second is at depths from 32 to 36 km approximately 10 km northeast of the summit and the third is at a 37 km depth, approximately 7 km northeast of the summit. In contrast, ILFs are located within a vertical pipe-like region just beneath the summit and sometimes show a vertical migration of the focal depth. Our moment tensor inversion using spectral ratios of body waves indicates that the source mechanisms of the DLFs and ILFs have a significant double couple and a compensated linear-vector dipole component. It is also found that a significant volumetric change is included in the source mechanisms for some DLFs. Such source mechanisms of DLFs and ILFs can be explained by the motion of a tensile crack coupled either with a shear crack or with an oblate spheroid magma chamber. However, the orientations and polarities of the crack motions are not the same in each region of DLFs and ILFs. These results suggest that a complex magma system is present at the source regions of the DLFs and ILFs.

Key words: earthquakes, magma, seismicity, source mechanism, spectral ratio.

1 INTRODUCTION

It is well known that low-frequency earthquakes (LFs) and tremors are observed in the deep crust and mantle beneath volcanoes, although the majority of LFs and tremors originate at depths of less than 3 km (McNutt 1994). For example, LFs at Kilauea volcano, Hawaii, occur at depths from 5 to 60 km (Koyanagi *et al.* 1987) and LFs beneath Hekla volcano, Iceland are found at depths from 8 to 14 km (Soosalu & Einarsson 1997). LFs occurring at deep portions beneath volcanoes have also been reported at other regions: Long Valley caldera (Pitt & Hill 1994), Spurr volcano, Alaska (Power *et al.* 1995), Izu-Ooshima volcano, central Japan (Ukawa & Ohtake 1987), and volcanoes in northeastern Japan (Hasegawa *et al.* 1991; Hasegawa & Yamamoto 1994). Following the study by Koyanagi *et al.* (1987), these LFs are often classified into two groups: intermediate-depth LF earthquakes (ILFs) that occur at depths from 5 to 15 km and deep LF earthquakes (DLFs) that occur at depths from 30 to 60 km.

To clarify the quantitative relationship between magmatic processes and DLFs and ILFs, previous studies have investigated the source mechanisms of such LFs. For example, Ukawa & Ohtake (1987) explained a DLF beneath Izu-Ooshima volcano by flow in a channel connecting two magma chambers. Nishidomi & Takeo (1996) obtained a focal mechanism of strike-slip type for a DLF near Nikko-Shirane volcano, Japan. Okada & Hasegawa (2000) obtained non-double-couple focal mechanisms for three DLFs near Narugo volcano, Japan. However, the number of estimated focal mechanisms of LFs for each volcanic region is few,

*Now at: Earthquake Research Institute, University of Tokyo, Tokyo 113-0032, Japan. E-mail: nakamiti@eri.u-tokyo.ac.jp

and no significant common features have been found in the focal mechanisms.

In 1998–1999, we observed many DLFs and ILFs at Iwate volcano (2038 m), one of several active Quaternary stratovolcanoes lying in the northeastern Japan arc (Fig. 1a). A remarkable volcanic tremor of 45 min duration was first observed on 1995 September 15 and initiated intensified ILF activity (Ueki *et al.* 1996). Although ILF and DLF activities were quite low for the period from 1996 to 1997, DLF activity intensified at the end of 1998 January. At that time, shallow high-frequency (SHF) earthquake swarms (Tanaka *et al.* 2002), very-long-period (VLP) seismic events (Nishimura *et al.* 2000) and crustal deformation were observed in the shallow part of the volcano (Sato & Hamaguchi 1999; Ueki *et al.* 1999; Miura *et al.* 2000), and these were considered to originate from intrusion of magmatic fluid (Sato & Hamaguchi 1999; Ueki *et al.* 1999; Miura *et al.* 2000; Tanaka *et al.* 2002). After a tectonic earthquake of local magnitude of 6.1 occurred at a shallow location adjacent to the volcano-seismic swarm area on 1998 September 3 (Umino *et al.* 1998; Nakahara *et al.* 2002), the ILF and DLF activities gradually weakened as did SHF, VLP and crustal deformation at the shallow location. During the 1998–1999 volcanic activity, we observed in total 350 DLFs and 120 ILFs.

In this study, we examined the DLFs and ILFs of Iwate volcano by analysing high-quality data obtained using our dense seismic network deployed around the volcano. First, we determined spatial-temporal variations of the hypocentre distributions of DLFs and ILFs using the joint hypocentre determination (JHD) method. Subsequently, we examined the source mechanisms of DLFs and ILFs beneath Iwate volcano, applying a spectral ratio method we have recently developed. In this paper, we discuss the implications of our results for the magmatic activity by comparing them with similar results from other volcanoes.

2 SEISMIC OBSERVATIONS ON AND AROUND IWATE VOLCANO

We analysed seismic data from 47 stations consisting of three seismic networks on and around Iwate volcano (Fig. 1): the permanent volcano seismic network of Tohoku University (crosses), a temporary reinforcing seismic network in operation since 1995 (diamonds) and a satellite-based temporary network of the Joint Seismic Observation (JOINT, solid squares) operated by a Japanese research group in the period from 1997 October to 1999 May (Hasegawa & Hirata 1999). Seismic signals transmitted from stations (solid circles) of the Japan Metrological Agency (JMA) by telephone line supplement the data set after 1997 October.

All of the stations in these networks are equipped with three-component seismometers. Most of the seismometers at these stations are short-period instruments with a natural period of $T_0 = 1$ s, but some of them are longer-period instruments with $T_0 = 5$ s (KRB, UEB and YKR), $T_0 = 20$ s (HAN, NSK and TAZ), and one is an STS-2 broad-band seismometer (IWT). The seismometers at the permanent stations are installed in boreholes at depths of either 300 or 557 m from the ground surface (ANS, GNB, HSB, YKB and MTO) together with tiltmeters and strainmeters, or in vaults at the ends of 5–50 m long tunnels. Most of the permanent stations have been in operation for more than 4 yr. The seismometers at the temporary stations are buried in soil or are attached to bedrock. Seismic data from the permanent stations are digitized by a 16 or 22 bit analogue-to-digital converter with a sampling frequency of 100 Hz, and are telemetered to Tohoku University in Sendai by telephone lines. Data from temporary stations IEF, IKG, KNS, OSD, RZT, SDF, UBK, UEB and YKR are telemetered to the university by radio and/or telephone lines with 12-bit resolution, and those from temporary station SZK and the JOINT stations are telemetered by a satellite system with 22-bit resolution (Urabe *et al.* 1998) to Tohoku University. Seismic signals from temporary stations KHM, KRB, SRY and TKM are continuously stored in a 2 GB hard disc at each site by a digital data recorder with 16-bit resolution and a sampling frequency of 100 Hz. The internal crystal clock of the recorder (precision better than 10^{-6} at -20 to $+40$ °C) is corrected every hour by a GPS time signal so that timing error is assured to be less than 4 ms.

3 HYPOCENTRE DISTRIBUTIONS OF DEEP AND INTERMEDIATE-DEPTH LOW-FREQUENCY EARTHQUAKES

3.1 Hypocentre distribution of deep low-frequency earthquakes

Recordings of DLFs beneath Iwate volcano generally show clear *P* and *S* waves (Figs 2a and b). We measured the arrival times of *P* and *S* phases of DLFs on the three-component seismograms and determined their hypocentres whenever the onsets of *P* and *S* waves were picked at five or more stations with good azimuthal coverage. The reading accuracies of *P* and *S* wave arrival times are better than ± 0.2 and ± 0.3 s, respectively. We located the hypocentres of 120 DLFs in the period from 1997 October to 2000 June, using the velocity model of Tanaka *et al.* (2002) and a standard hypocentre determination procedure. The results show that 90 DLFs are concentrated beneath the southern flank of the volcano (south DLFs), and the other 30 DLFs occur beneath the northeastern flank (northeast DLFs). The local magnitudes of the DLFs are distributed in the range 0.5–2.1. Since both DLF groups are concentrated tightly in their respective regions, we apply the JHD method (Douglas 1967; Pujol 1988) separately to the south and the northeast DLFs. Fig. 3 shows hypocentres relocated by the JHD method. The south DLFs are concentrated at depths from 31 to 34 km. Their epicentres form a dense spherical cluster beneath the south flank approximately 10 km from the summit. We call these earthquakes group A. Conversely, hypocentres of the northeast DLFs are divided into two groups, B and C. Group B earthquakes are concentrated at depths from 32 to 36 km approximately 10 km northeast of the summit, while group C earthquakes are located at depths around 37 km approximately 7 km northeast of the summit. Group C earthquakes are significantly deeper than group B earthquakes, because *S*–*P* times for group B (4.0 s) are shorter than those for group C (4.7 s) at the nearest station SRY. Taking the reading errors of the arrival times into account, we estimate the typical location errors to be less than approximately 1.5 km in both horizontal and vertical directions. The mean and standard deviations of rms residuals of *P* and *S* phases for the relocated northeast DLFs are 0.09 ± 0.05 s and 0.10 ± 0.04 s, respectively, and those for the relocated south DLFs are 0.12 ± 0.07 and 0.13 ± 0.06 s, respectively. Because the rms residuals of *P* and *S* phases obtained by the JHD method are reduced to 50 and 70 per cent of those obtained by the ordinary method, respectively, the hypocentres determined by the JHD method are more reliable.

3.2 Hypocentre distribution of intermediate-depth low-frequency earthquakes

Recordings of ILFs beneath Iwate volcano also generally show clear *P* and *S* waves (Fig. 2c), hence we determine their hypocentres

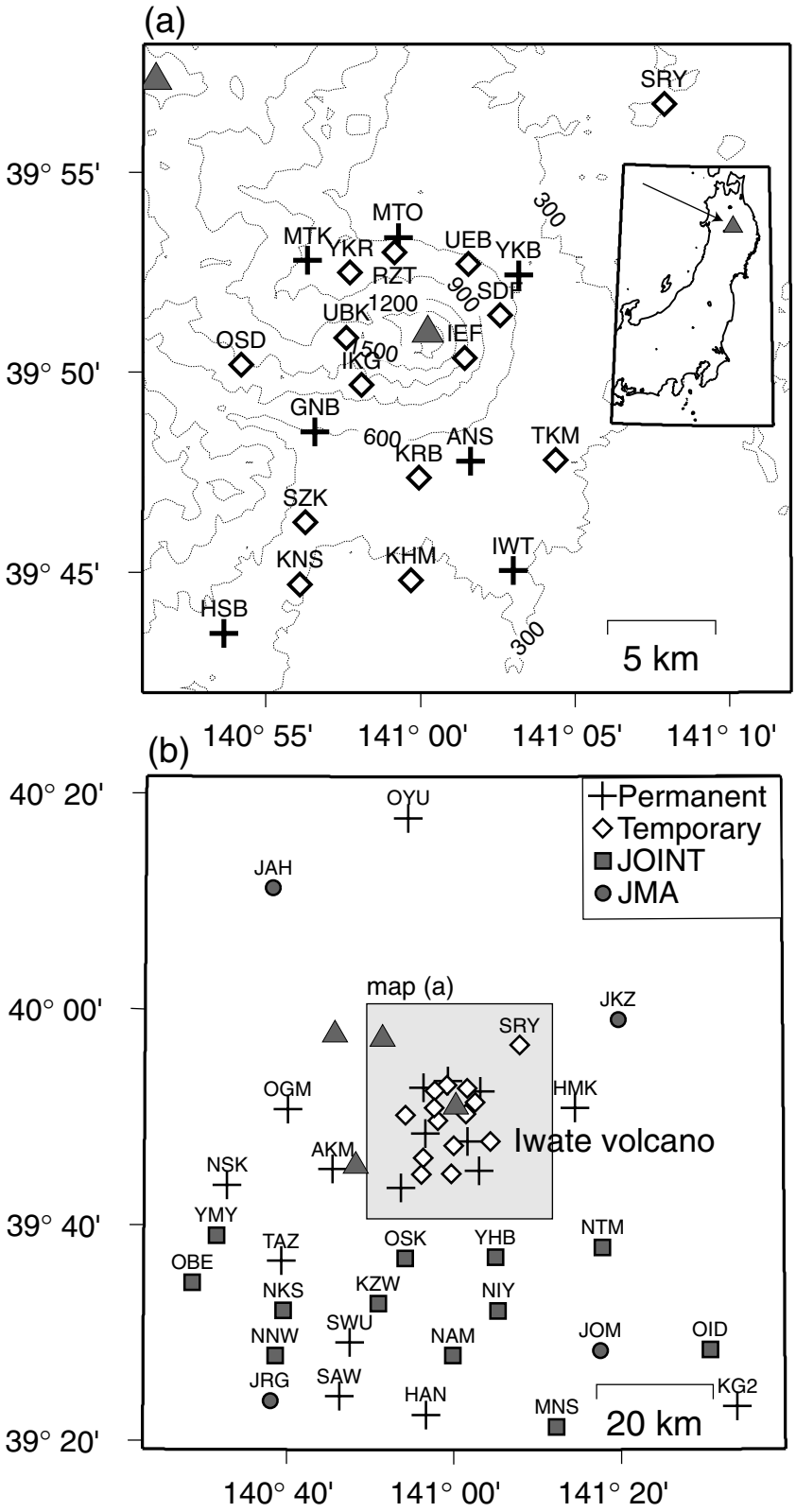

Figure 1. Location map showing the seismic stations. (a) Stations near Iwate volcano and location of Iwate volcano (inset map). (b) Stations around the volcano. The various symbols in the figure denote different types of station: crosses, permanent stations maintained by Tohoku University; diamonds, temporary stations maintained by Tohoku University; squares, temporary stations maintained by the joint seismic observations of Japanese universities (JOINT); solid circles: stations maintained by the Japan Meteorological Agency (JMA). Triangles denote active volcanoes. Dotted lines in (a) show elevation contours at 300 m intervals.

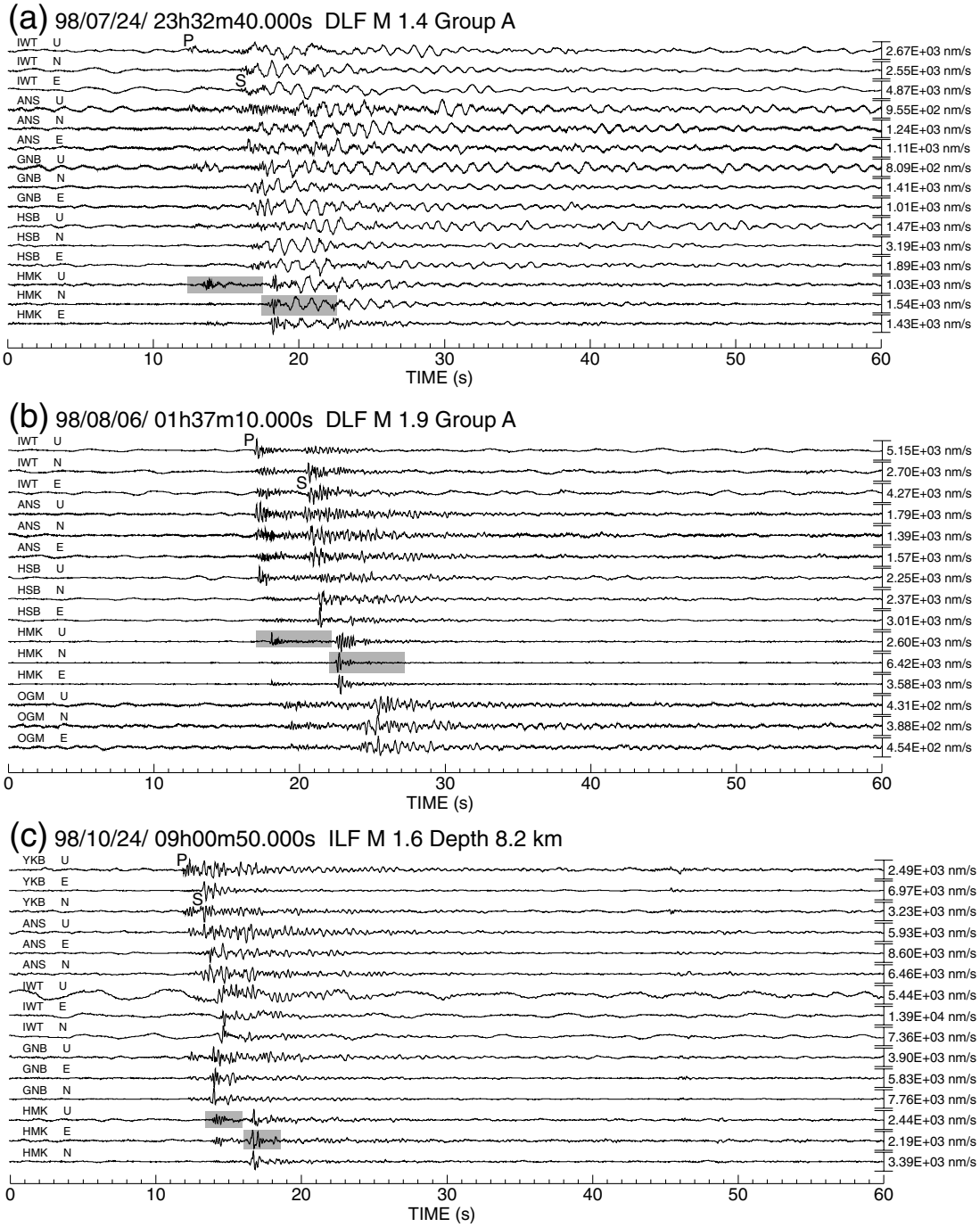

Figure 2. (a) An example of three-component waveforms for the south DLFs from an earthquake which occurred at 23:32 JST on 1998 July 24. This earthquake is characterized by high-frequency onsets and monotonic coda waves. (b) Same as (a) for the earthquake at 01:37 on 1998 August 6. This DLF has the best signal-to-noise ratio we have observed since 1981. The *S*- to *P*-wave amplitude ratios differ from station to station. (c) An example of three-component waveforms for the ILF earthquake which occurred at 9:01 JST on 1998 October 24. The *S*- to *P*-wave amplitude ratios differ from station to station. Shaded rectangles on the waveforms of HMK represent the time windows for calculating the spectra shown in Fig. 4.

when the onsets of *P* and *S* phases are available for at least four and seven stations, respectively. The reading accuracies of both *P* and *S* wave arrival times are better than ±0.1 s. We located 139 ILFs during the period from 1998 April to 2000 June. The local magnitudes of ILFs are distributed in the range 0.0–1.6. Since the hypocentres determined by the standard method are concentrated in a small region, we applied the JHD method to the ILFs, too. Their hypocentres are shown in Fig. 3 together with those of the DLFs. The ILFs are located within a nearly vertical cylindrical or pipe-like region extending from 5 to 12 km in depth, with north–south and east–west dimensions of approximately 1.5 and 1.7 km, respectively. The vertical distribution from 5 to 12 km in Fig. 3 is not due to mislocations, because *S*–*P* times at station YKB, which is located just above the hypocentres, vary from 0.9 to 1.6 s. The mean

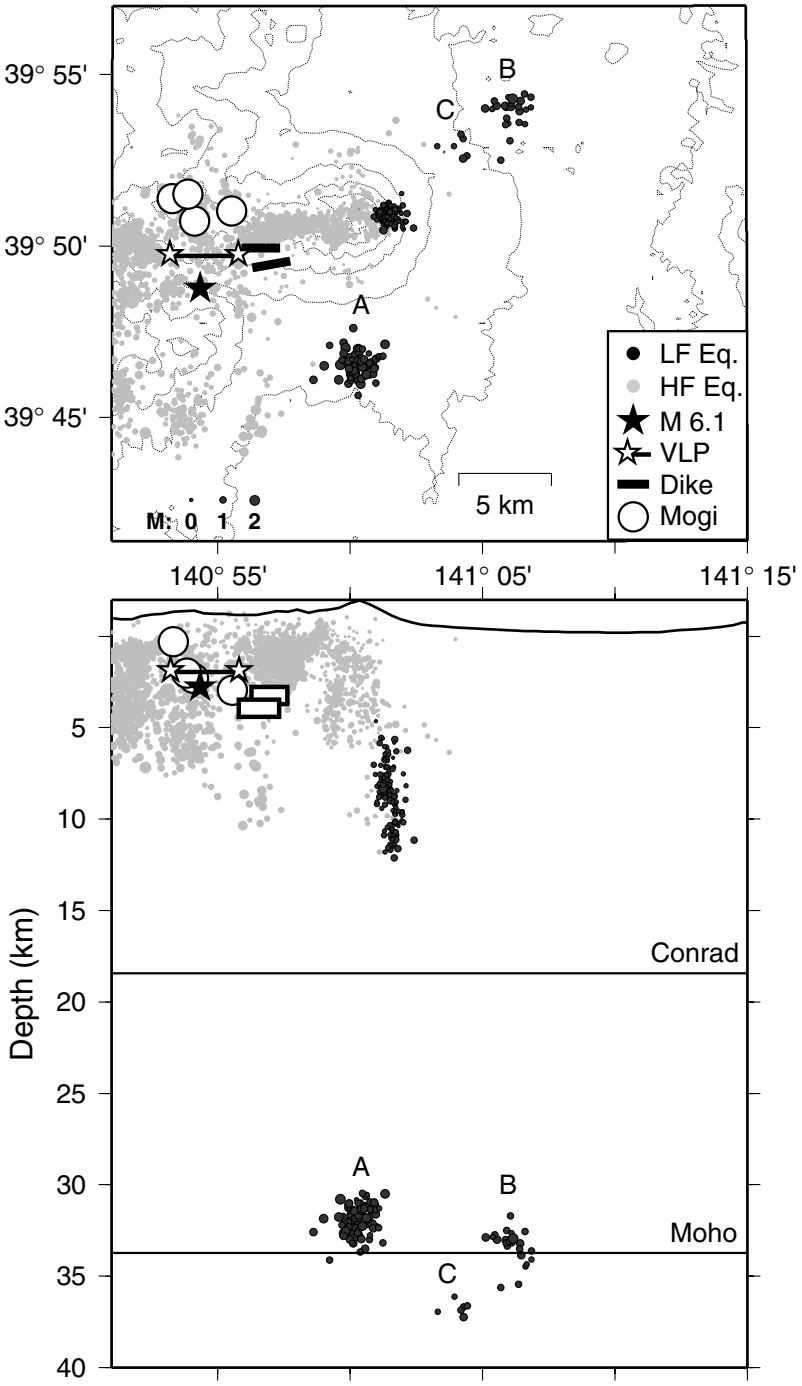

Figure 3. Epicentres and cross-sections of hypocentres of DLFs and ILFs (solid circles), as determined by the JHD method. HF earthquakes (light grey circles) in the period from 1997 December to 2000 June are also shown. The solid star marks the initial rupture point of the $M = 6.1$ earthquake. The locations of very-long-period events (Nishimura *et al.* 2000), dykes and Mogi sources estimated from GPS data (Miura *et al.* 2000) are also shown. The Conrad and Moho depths are shown with solid lines (Nakajima *et al.* 2001). The local magnitudes of DLFs and ILFs range from 0.5 to 2.1 and 0.0 to 1.6, respectively. The hypocentres of DLFs are separately located within the three regions: group A, B and C. The ILFs define a pipe-like distribution. Elevation contours (dotted lines) are at 300 m intervals. The cross-sections are free of any vertical exaggeration.

values and standard deviations of residuals of *P* and *S* phases using the JHD method are 0.09 ± 0.03 and 0.10 ± 0.04 s, respectively. The rms residuals of *P* and *S* phases obtained by the JHD are reduced to 70 and 40 per cent of those obtained using the standard method, respectively. The residuals obtained by the JHD method are almost within the picking accuracy of the *P* and *S* phases.

4 WAVEFORM CHARACTERISTICS OF DEEP AND INTERMEDIATE-DEPTH LOW-FREQUENCY EARTHQUAKES

Fig. 2 shows examples of three-component waveforms of DLFs and ILFs at five stations. Fig. 2(a) shows an example of DLFs in

group A that have a monotonic *S* coda with a dominant frequency of approximately 1 Hz. Amplitudes of the 1 Hz monotonic long *S* coda seem to be similar at all stations so the source mechanism of this DLF cannot consist of a pure double-couple or it is purely isotropic, but it must have some volumetric component. High-frequency waves are clearly seen in the onset of *P* and *S* waves at stations located close to the epicentre of this earthquake (e.g. ANS, IWT, GMB, HSB and HMK). Fig. 2(b) shows a DLF ($M = 1.9$) in group A, which occurred at 01:37 on 1998 August 6. This earthquake has the largest signal-to-noise ratio we have observed since 1981. The dominant frequencies of *P* and *S* waves for this earthquake are approximately 5 Hz. Amplitudes of *P* and *S* waves for this earthquake differ from station to station. These characteristics are quite different from those of the DLF shown in Fig. 2(a). Hence, the waveforms of the DLFs cannot be characterized as a single earthquake family, even though the DLFs in group A are clustered in a small region of approximately 1.5 km in radius. This suggests that the variety of waveforms is caused mainly by a variety of source processes and not by path or site effects.

Fig. 2(c) shows an example of ILFs ($M = 1.6$), which occurred at 9:01 on 1998 October 24. The amplitudes of *S* waves are larger than those of *P* waves. As shown in Fig. 2(c), ILFs typically generate significant *S* waves. The amplitudes of *S* waves differ from station to station, which implies that the source mechanism is not explained by a pure isotropic explosion or implosion. It should be noted that no ILFs have monotonic long *S* coda waves.

We examine velocity amplitude spectra for all DLFs and ILFs from vertical and N–S components at station HMK (Fig. 4). The dominant frequencies of *P* and *S* waves range from 1 to 8 Hz and from 1 to 6.5 Hz, respectively. Most of the dominant *P* wave

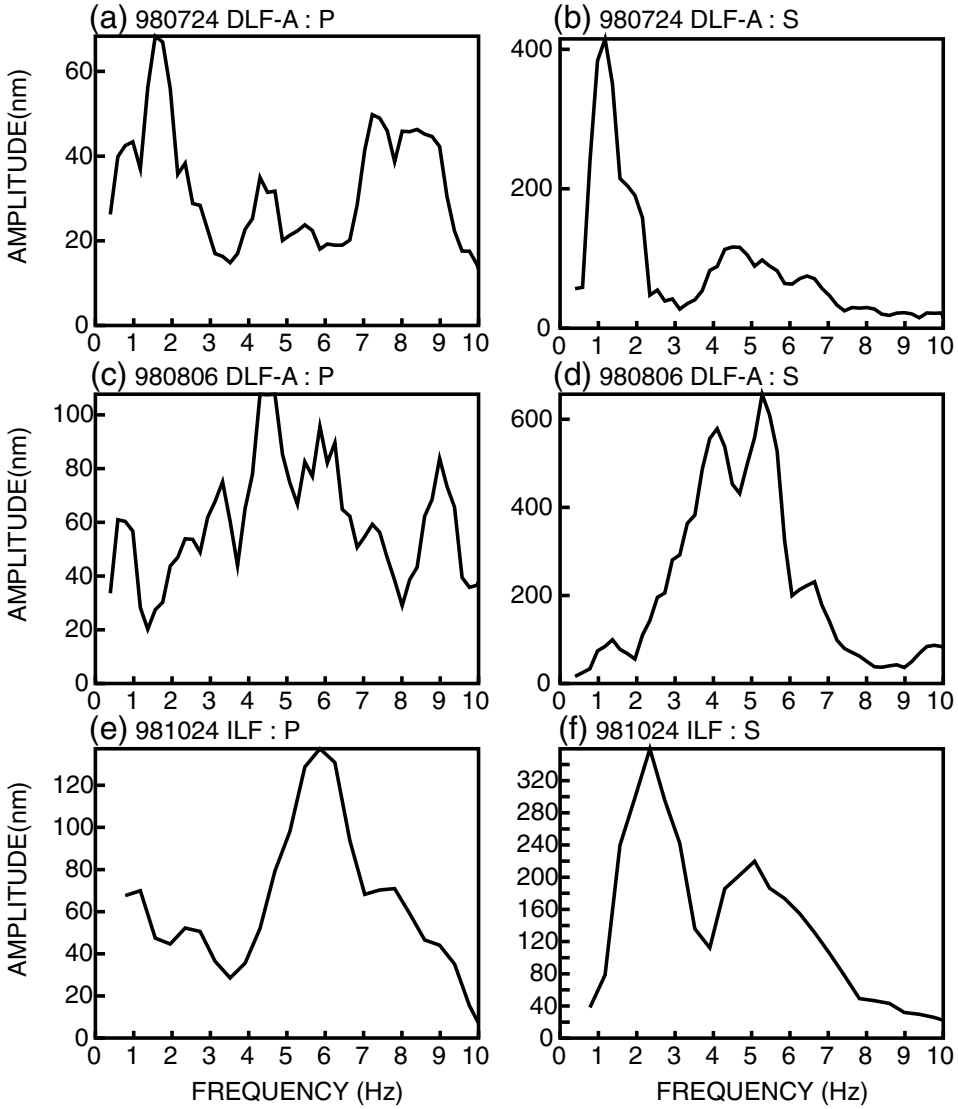

Figure 4. Velocity amplitude spectra at HMK for DLFs and ILFs shown in Fig. 2. The window lengths for DLFs and ILFs are 5.12 and 2.56 s, respectively. The corresponding time windows are indicated by the shaded rectangles in Fig. 2. (a) Spectrum of the vertical component for the *P* wave in Fig. 2(a) showing dominant peaks at approximately 1.5 and 7 Hz. (b) Spectrum of the NS component for the *S* wave in Fig. 2(a) showing a dominant peak at approximately 1 Hz. (c) Spectrum of the vertical component for the *P* wave in Fig. 2(b) showing dominant peaks at approximately 4.5, 6 and 9 Hz. (d) Spectrum of the NS component for the *S* wave in Fig. 2(b), showing dominant peaks at approximately 4 and 5 Hz. (e) Spectrum of the vertical component for the *P* wave in Fig. 2(c), showing a dominant peak at approximately 6 Hz. (f) Spectrum of the NS component for the *S* wave in Fig. 2(c), showing dominant peaks at approximately 2 and 5 Hz.

frequencies are estimated to be 2.5–5.0 Hz. Approximately 30 per cent of DLFs have *S* waves with a dominant frequency of 1 Hz; the remainders have dominant frequencies from 2 to 6 Hz. Dominant frequencies for ILFs are distributed widely, ranging from 1 to 8 Hz for *P* waves, and from 1 to 6 Hz for *S* waves. Only 1 per cent of ILFs have dominant frequencies around 1 Hz, which contrasts with the frequency spectrum found for DLFs.

5 SOURCE MECHANISMS OF DEEP AND INTERMEDIATE-DEPTH LOW-FREQUENCY EARTHQUAKES

5.1 Body wave spectral ratio method

We applied a body wave spectral ratio method to determine the source mechanisms of DLFs and ILFs, because the method has the advantage that a source time function does not need to be postulated before the inversion (e.g. Nishimura *et al.* 1995). The body wave spectral ratio method used in this study is as follows: we assume that the source sizes of earthquakes are small compared with the wavelength of the seismic waves analysed, allowing a point source approximation (Aki & Richards 2002). Assuming that all components of moment tensors have the same source time function with different amplitudes, the *n*th component of displacement at a location **x** can be written as

$$u_n(\mathbf{x}, t) = \sum_{p,q} M_{pq} S(\tau) * G_{np,q}(\mathbf{x}, t; \tau), \tag{1}$$

where M_{pq} is the pq element of the moment tensor, $S(\tau)$ is the source time function and $G_{np,q}(\mathbf{x}, t; \tau)$ is the np element of the Green function that relates the nth component of the displacement at the receiver position **x** with the pth component of impulsive force acting at the source position at time $t = \tau$. The notation ,q implies spatial differentiation with respect to the q coordinate and the asterisk denotes convolution.

Denoting far-field *P*, *SV* and *SH* displacements as $u_v^P(t)$, $u_r^{SV}(t)$ and $u_t^{SH}(t)$, respectively, and taking spectral ratios between the three displacements, we can obtain the body wave spectral ratios:

$$R^{SV/P}(\omega) = \frac{u_r^{SV}(\omega)}{u_v^P(\omega)} = \frac{\sum_{p,q} M_{pq} G_{rp,q}^{SV}(\omega)}{\sum_{p,q} M_{pq} G_{vp,q}^{P}(\omega)},$$

$$R^{SH/P}(\omega) = \frac{u_t^{SH}(\omega)}{u_v^P(\omega)} = \frac{\sum_{p,q} M_{pq} G_{tp,q}^{SH}(\omega)}{\sum_{p,q} M_{pq} G_{vp,q}^{P}(\omega)},$$

$$R^{SH/SV}(\omega) = \frac{u_t^{SH}(\omega)}{u_r^{SV}(\omega)} = \frac{\sum_{p,q} M_{pq} G_{tp,q}^{SH}(\omega)}{\sum_{p,q} M_{pq} G_{rp,q}^{SV}(\omega)}, \tag{2}$$

where subscripts v, r and t denote the vertical, radial and transverse components, respectively. $R^{SV/P}$, $R^{SH/P}$ and $R^{SH/SV}$ are the body wave spectral ratios for the three combinations and are no longer dependent on the source time functions. The body wave spectral ratio $R^{l/m}(\omega)$ can be rewritten as

$$R^{l/m}(\omega) = A^{l/m}(\omega) \exp[i\theta^{l/m}(\omega)], \tag{3}$$

where $A^{l/m}(\omega)$ and $\theta^{l/m}(\omega)$ are the amplitude ratio and phase difference, respectively. l and m refer to the body wave type, *P*, *SV* and *SH*.

We estimate the source mechanisms of DLFs and ILFs by comparing the observed spectral ratios with theoretical ones. First, we explain data processing for the observed DLFs. Observed waveforms are bandpass filtered using the fourth-order filter with a zero-phase shift in the range from 0.7 to 8.0 Hz. Subsequently, we resample the data to a sampling rate of 50 s^{-1}, and rotate the data to radial and transverse components. Then, we set a time window with a 10 per cent cosine taper for the three-component data, slightly before the arrivals of the *P* or *S* waves. The length of the time window is set to be 0.64, 1.28 or 2.56 s, corresponding to two or three cycles of the *S* wave. Fig. 5 shows examples of the time windows for vertical, radial and transverse components of DLFs. Finally, we take the Fourier transform of the *P*, *SV* and *SH* waves using the fast Fourier transform (FFT) method and calculate the amplitude ratios and the phase differences between the two components.

Next, we calculate the theoretical spectral ratio. We calculate Green's functions for a given moment tensor, $\boldsymbol{M} = M_0(m_{xx}, m_{yy}, m_{zz}, m_{xy}, m_{yz}, m_{zx})$, where M_0 is the amplitude of seismic moment and the m_{ij} take values from -1 to 1, using the discrete wavenumber method (Bouchon 1979, 1981) and reflection and transmission coefficient matrices (Kennett & Kerry 1979). In the calculation, we assume a layered structure as shown in Nakamichi (2000). This structure is based on the velocity structure of Tanaka *et al.* (2002) and the attenuation structure of Tsumura *et al.* (2000). The location of each source is set at the hypocentre determined by the JHD method. Then, we compute synthetic waves in the time domain for an assumed source mechanism by superimposing the Green functions for the six components of the moment tensor. Following the processing procedure for the observed data discussed previously, we obtain the amplitude ratios and the phase differences between the two components.

We represent the observed amplitude ratio and phase difference by $A_{\rm obs}^{i,j}(\omega)$ and $\theta_{\rm obs}^{i,j}(\omega)$, respectively, and the theoretical equivalents by $A_{\rm cal}^{i,j}(\omega; \boldsymbol{M})$ and $\theta_{\rm cal}^{i,j}(\omega; \boldsymbol{M})$. The superscript i denotes a station and j indicates SV/P, SH/P or SH/SV. Then, the weighted sum of squared mean residuals of the amplitude ratios and phase differences can be expressed as

$$S(\mathbf{M}) = \sum_{i=1}^{N}\sum_{j=1}^{3}\sum_{k=1}^{K}\left[\log_{10} A_{\rm obs}^{i,j}(\omega_k) - \log_{10} A_{\rm cal}^{i,j}(\omega_k; \mathbf{M})\right]^2 \Big/ 3NK + w_P \sum_{i=1}^{N}\sum_{j=1}^{3}\sum_{k=1}^{K}\left[\theta_{\rm obs}^{i,j}(\omega_k) - \theta_{\rm cal}^{i,j}(\omega_k; \mathbf{M})\right]^2 \Big/ 3NK, \tag{4}$$

where ω_k is the discretized angular frequency, N is the number of stations and K is the total number of angular frequencies used for the calculation. w_P is the weighting factor and determines the relative importance of the amplitude and phase residuals. We obtain the best-fitting moment tensor solutions that satisfy

$$S(\mathbf{M}) \rightarrow \min. \tag{5}$$

When the ratio of *P* and *S* wave velocities is nearly constant in the crust, amplitude ratios are relatively insensitive to crustal heterogeneities, although seismic-wave amplitudes are strongly distorted by them (e.g. Julian & Foulger 1996). On the other hand, phase differences are sensitive not only to crustal heterogeneities but also to the finite spectral window chosen. Therefore, we set the weighting factor w_P to be small, varying from 0 to 0.05.

The amplitude spectra of the observed *P*, *SV* and *SH* waves at each station are normalized and stacked to obtain the average amplitude spectra for *P*, *SV* and *SH* waves at each station. We analyse only the spectral ratios in a limited frequency band in which the spectral amplitude is larger than or equal to half the overall maximum of the amplitude spectra of *P*, *SV* and *SH* waves. The frequency bands are calculated by this criterion for the *P*, *SV* and *SH* waves, independently, and all frequency bands common to the three are used to optimize eq. (4).

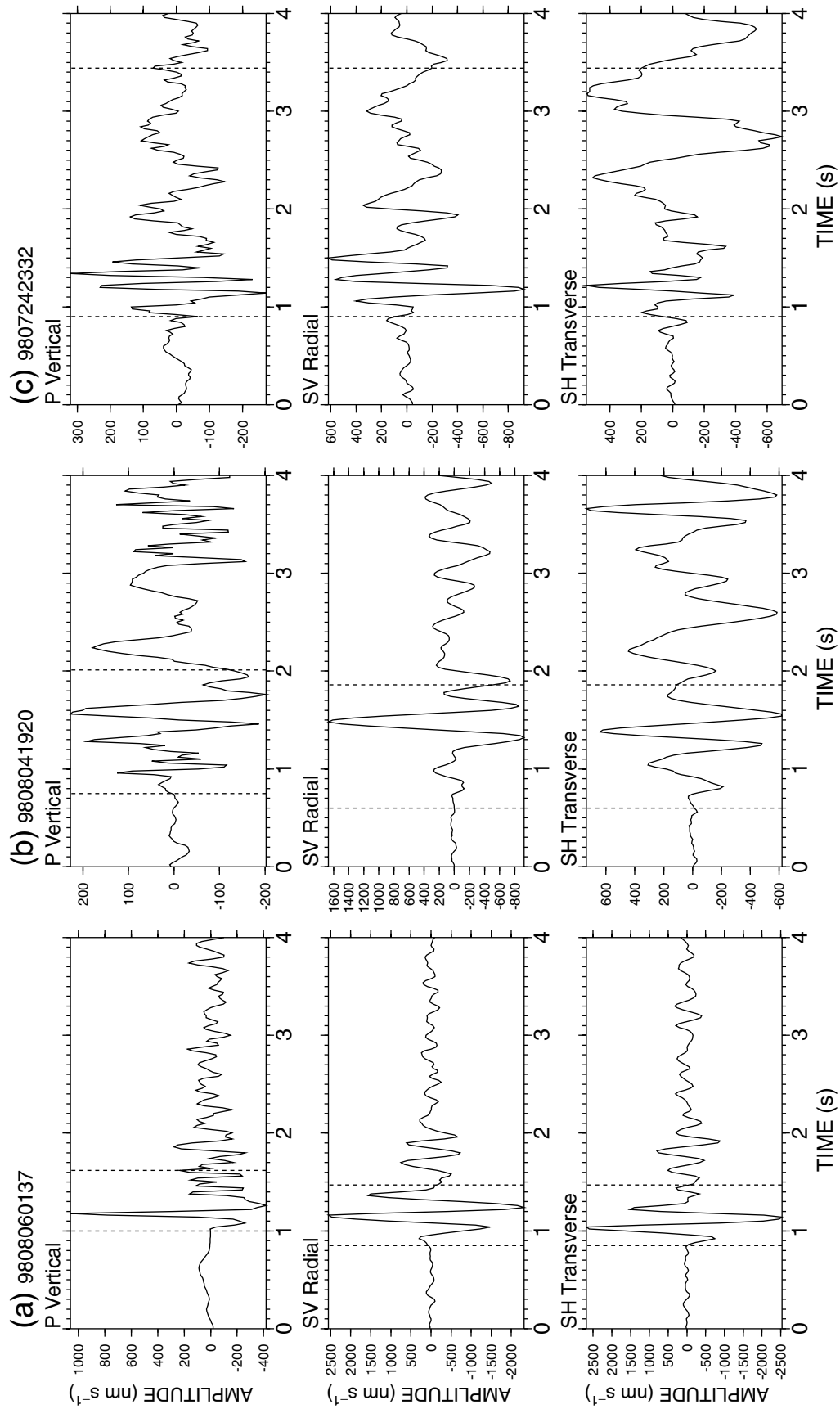

Figure 5. Examples of vertical, radial and transverse components of *P*, *SV* and *SH* waves. Dotted lines in each trace indicate the time windows for calculating the spectral ratios. (a) DLF at 1:37 1998 on August 6. The window length is 0.64 s. (b) DLF at 19:20 on 1998 August 4. The window length is 1.28 s. (c) DLF at 23:32 on 1998 July 24. The window length is 2.56 s.

Table 1. Relative moment tensor components estimated by the spectral ratio method for deep low-frequency events and weights for phase difference.

Event ID	Date	Time	M	Group*	N	m_{xx}	m_{yy}	m_{zz}	m_{xy}	m_{yz}	m_{zx}	w_P
DLFA-1	06/06/98	07:04	2.0	A	19	−0.171	−0.130	0.698	0.542	0.195	0.634	0.01
						(0.097)	(0.477)	(0.242)	(0.283)	(0.113)	(0.233)	
DLFA-2	07/24/98	23:32	1.4	A	27	−0.572	−0.684	−0.045	−0.138	−0.280	0.710	0.05
						(0.072)	(0.115)	(0.053)	(0.086)	(0.097)	(0.248)	
DLFA-3	08/04/98	19:20	1.5	A	29	−0.255	0.695	0.489	−0.102	0.730	−0.251	0.02
						(0.103)	(0.049)	(0.057)	(0.129)	(0.026)	(0.051)	
DLFA-4	08/06/98	01:37	1.9	A	25	−0.164	0.802	−0.590	−0.475	0.481	−0.183	0.01
						(0.131)	(0.095)	(0.130)	(0.065)	(0.109)	(0.040)	
DLFA-5	01/03/99	04:05	1.3	A	22	0.565	0.659	−0.532	−0.482	0.442	0.232	0.02
						(0.101)	(0.019)	(0.027)	(0.069)	(0.073)	(0.020)	
DLFB-1	05/30/98	09:57	1.4	B	13	0.507	0.323	−0.623	0.727	0.042	−0.307	0.00
						(0.055)	(0.120)	(0.043)	(0.045)	(0.052)	(0.026)	
DLFC-1	03/20/98	22:51	1.5	C	24	0.255	−0.529	0.214	−0.665	−0.159	−0.580	0.05
						(0.033)	(0.034)	(0.026)	(0.043)	(0.036)	(0.022)	

x-axis directed north, y-axis directed east, z-axis directed down. Each moment tensor component is normalized with respect to the scalar moment defined by Dahlen & Tromp (1998). The numerical values in parentheses indicate the estimated standard errors for the moment components. M, magnitude; N, number of stations used for the inversion. *Group is defined in the text (see Fig. 3).

To estimate the moment tensor **M**, we need to minimize $S(\mathbf{M})$. However, eq. (2) has a strong non-linearity and the number of free parameters (six) is too large to use a general grid searching method. We therefore use a genetic algorithm (Holland 1975; Goldberg 1989) that is useful for solving highly non-linear problems, including some geophysical inverse problems (e.g. Sen & Stoffa 1992; Sambridge & Drijkoningen 1992; Sambridge & Gallagher 1993). In our genetic algorithm inversion, each moment tensor component (m_{ij}) is allowed to vary from –1.0 to 1.0 and the increment of each component is 0.065.

We obtain moment tensor solutions for weighting factors, w_P, of 0.00, 0.01, 0.02, 0.03, 0.04 and 0.05. Finally, we select the moment tensor solution that satisfies the P wave first-motion polarities as consistently as possible. After making all the calculations, we found that the moment tensor solutions of the DLFs and ILFs do not depend significantly on the weighting factors w_P used. We also estimated the covariance matrix for an estimated moment tensor using an *a posteriori* Gaussian probability density function obtained from the genetic algorithm inversion. The standard deviations are the square roots of the diagonal terms of the covariance matrix (Tables 1 and 2). Tables 1 and 2 show the best moment tensors selected as above for DLFs and ILFs with the standard deviations of the solutions, respectively.

5.2 Source mechanisms of deep low-frequency earthquakes

To obtain a well-constrained source mechanism, we select DLFs with: (1) local magnitudes greater than or equal to 1.0; (2) good signal-to-noise ratios in all three components for at least 16 stations (south DLFs) or at least 11 stations (northeast DLFs); (3) good azimuthal and distance coverage. As a result, five south DLFs and two northeast DLFs were selected out of the total 120 DLFs (see Table 1).

Fig. 6 compares the observed amplitude spectral ratios with the theoretical equivalents for the best-fitting moment tensor solution of DLFA-2 at 21 stations (see Table 1). Figs 7(a)–(g) and Table 1 summarize the moment tensor solutions of the seven DLFs. We do not show the phase difference data because the weights for the phase data are very small compared with the amplitude ratios. As shown, especially in Fig. 7(e), P wave first-motion polarities of the earthquake are very consistent with the best-fitting moment tensor solution. This demonstrates that our moment tensor inversion method is very useful for estimating the moment tensor solutions of DLFs.

The source mechanisms are significantly different from each other (Fig. 7), which is consistent with the result that no earthquake families are observed (Nakamichi 2000). No characteristic orientation of the principal axes of the moment tensors of DLFs is found. To investigate the characteristics of the moment tensors, we decomposed the moment tensors into three elementary force systems that consist of isotropic (volumetric), double-couple (DC) and compensated linear-vector dipole (CLVD) force systems. This decomposition is useful for interpreting DLF source mechanisms: the volumetric component represents a spherical magma oscillation (Crosson & Bame 1985; Julian *et al.* 1998; Miller *et al.* 1998); the DC component is a manifestation of shear faulting (Natale *et al.* 1995; Julian *et al.* 1998; Miller *et al.* 1998), and the CLVD represents rapid movement of magmatic fluid (Julian & Sipkin 1985; Kanamori *et al.* 1993; Julian *et al.* 1998; Miller *et al.* 1998). The decompositions are performed using the method of Knopoff & Randall (1970), which makes the major axis of the CLVD coincide with the corresponding axis of the DC. Decompositions of the moment tensor components for the DLFs are summarized in Fig. 7 and Table 3. Most of the source mechanisms of DLFs have significant DC (21–80 per cent) and CLVD (18–65 per cent) components. The source mechanisms of DLFA-3 and DLFA-5 have significant volumetric components and the source mechanism of DLFA-2, in particular, has a large volumetric component (31 per cent).

5.3 Source mechanisms of intermediate-depth low-frequency earthquakes

We selected four ILFs to estimate their source mechanisms according to the following criteria: (1) local magnitudes greater than or equal to 1.0, (2) good signal-to-noise ratios in all three components at over six stations and (3) a suitable azimuth and distance coverage of stations. The earthquakes selected are listed in Table 2.

We adopted a 0.64 s time window with a 10 per cent cosine taper, which contains one or two cycles of waves at the dominant frequency. The spectral ratios for P, SV and SH waves are calculated using the procedure for DLFs. The frequency bands used for the moment

Table 2. Relative moment tensor components estimated by the spectral ratio method for intermediate-depth low-frequency events and weights for phase difference.

Event ID	Date	Time	M	Depth (km)	N	m_{xx}	m_{yy}	m_{zz}	m_{xy}	m_{yz}	m_{zx}	w_P
ILF-1	06/28/98	17:46	1.0	5.7	7	0.569	−0.503	−0.185	0.466	−0.691	0.030	0.01
						(0.034)	(0.072)	(0.004)	(0.025)	(0.046)	(0.014)	
ILF-2	08/08/98	10:58	1.5	6.7	9	−0.543	0.231	0.047	−0.648	0.356	0.528	0.01
						(0.030)	(0.013)	(0.045)	(0.011)	(0.005)	(0.020)	
ILF-3	10/24/98	09:01	1.6	8.2	18	−0.623	0.037	0.739	0.577	−0.192	0.403	0.02
						(0.049)	(0.033)	(0.041)	(0.020)	(0.009)	(0.032)	
ILF-4	12/25/99	19:34	1.5	8.4	11	−0.463	0.732	−0.282	0.589	−0.056	0.485	0.05
						(0.055)	(0.026)	(0.233)	(0.093)	(0.235)	(0.126)	

x-axis directed north, y-axis directed east, z-axis directed down. Each moment tensor component is normalized with respect to the scalar moment defined by Dahlen & Tromp (1998). The numerical values in parentheses indicate the estimated standard errors for the moment components. M, magnitude; N, number of stations used for the inversion. MT, moment tensor inversion; SF, single-force inversion.

tensor inversion were also determined using the method described previously. Figs 7(h)–(k) show the estimated source mechanisms and the polarities of *P* wave first motions for the four selected ILFs. The source mechanisms differ from event to event and it is difficult to find a systematic feature in the principal axes of the moment tensors for all the ILFs. In general, the estimated source mechanisms match the polarities of *P* wave first motion well. In Fig. 8, the observed amplitude ratios are compared with the best-fitting theoretical ratios for ILF-3 at 12 stations. On the whole, the theoretical amplitude ratios fit the observed ones fairly well, except for the *SV* to *P* and *SH* to *P* amplitude ratios at IEF. No significant volumetric components are confirmed in the source mechanisms for the four ILFs (Table 3). These earthquakes show a significant DC (21–97 per cent) component and ILF-1, ILF-2, ILF-3 and ILF-4 show a CLVD (45–72 per cent) component.

6 DISCUSSION

6.1 Reliability of the source mechanisms of deep low-frequency earthquakes

We have represented the source mechanisms of DLFs and ILFs by six-component moment tensors. However, as pointed out by Ukawa & Ohtake (1987), a single force may be a dominant source for the magma movement in the crust. We carry out a grid search inversion in which single forces, instead of six moment tensor components, are determined using an optimizing equation. We use the Akaike Information Criterion (AIC) (e.g. Akaike 1973; Sakamoto *et al.* 1986) to test the significance of the difference. For the case of a normal distribution of errors, the AIC parameter is expressed as $\mathrm{AIC} = N' \ln(2\pi) + N' \ln S + N' + 2(m+1)$, where N', S and m are the number of data for the amplitude ratios and the phase differences, the sum of the squared mean residuals, and the number of model parameters, respectively. In the present study, $N' = 6NK$, where N is the number of stations, and K is the number of frequencies; $m = 6$ for the moment tensor and $m = 3$ for the single force. The AIC values calculated for the best moment tensor and single-force models for DLFs and ILFs are listed in Table 3. Since the values of AIC of the moment tensor models are smaller than those of the single-force models, we conclude that the difference is significant and that the moment tensor models are preferable.

A double-couple mechanism may represent the source mechanism of DLFA-4, because almost all *P* phase polarities can be explained by a normal fault mechanism as shown in Fig. 9. We therefore compare the residuals (eq. 4) and AIC values for the best moment tensor model with those for the normal fault model. The residual and the AIC value for the best moment tensor model are 0.294 and 1319, respectively. On the other hand, the residual and the AIC value for the normal fault model are 0.405 and 1575. Since the model with the smaller AIC value is statistically better, we conclude that the moment tensor model is a more plausible representation of the source mechanism of DLFA-4 than the normal fault model.

6.2 Source process for low-frequency earthquakes

As mentioned previously, the source mechanisms of DLFs and ILFs contain DC and CLVD components and DLFA-2, DLFA-3 and DLFA-5 include significant volumetric components. For an earthquake having all three components, i.e. DC, CLVD and volumetric components, a tensile–shear coupled source may be an appropriate model. Hill (1977) first presented the basic idea of a fracture network to explain earthquake swarms around volcanoes. Shaw (1980) proposed that magma is injected into the lithosphere by a process analogous to hydraulic fracturing. His model consists of a fracture network of magma-filled tensile cracks coupled with shear cracks, and magma migrates upward through the network of tensile and shear cracks. Shimizu *et al.* (1987) first proposed a seismic source model of a tensile–shear crack to explain the waveform of volcanic earthquakes observed at Miyake Island, Japan. We expect that a similar phenomenon may occur in the source region of DLFs and ILFs beneath Iwate volcano. That is, when the magma fluid pressure is high enough to produce brittle fractures, both tensile and shear faulting occur simultaneously or successively to generate the DLFs or ILFs. As a result, the source mechanism of the DLFs and ILFs has DC, CLVD and volumetric components. However, some DLFs and ILFs show no significant volumetric component in their source mechanisms. Thus, we must consider the reason for absence of volumetric components, that is, the mechanism of generating CLVD components with magma-filled tensile faulting.

When tensile faulting occurs in a fracture system under high fluid pressure, often associated with dyke intrusion (Julian 1983; Aki 1984; Julian & Sipkin 1985), some other process, such as fluid flow, must compensate the volumetric component expected from a tensile fault. At depths greater than a few kilometres, rocks cannot sustain high tensile stresses, especially those accompanying the creation of a void. Hence, a tensile crack can be created only in the case where a fluid under high pressure flows into it. A tensile crack in an isotropic medium can be represented by a point-force system with three mutually orthogonal dipoles: the diagonal components of the moment are $(\lambda + 2\mu)$, λ and λ, where λ and μ are Lamé

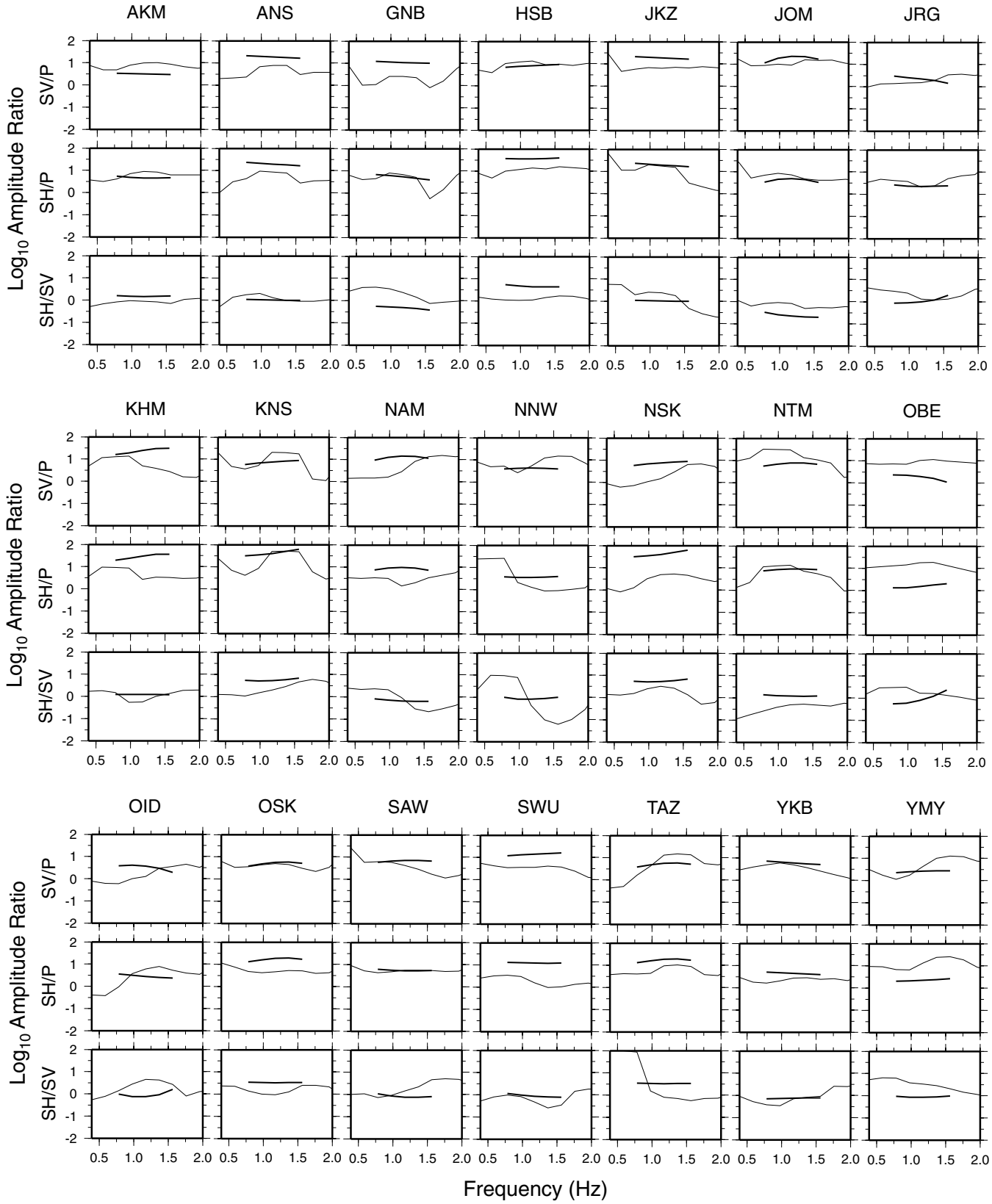

Figure 6. Comparisons of the observed amplitude spectral ratios (thin lines) to the theoretical amplitude spectral ratios (thick lines) of the best-fitting moment tensor solution for DLFA-2. The frequency ranges used for inversion are denoted by a range of theoretical ratios. On the whole, the theoretical amplitude ratios fit the observed ones closely.

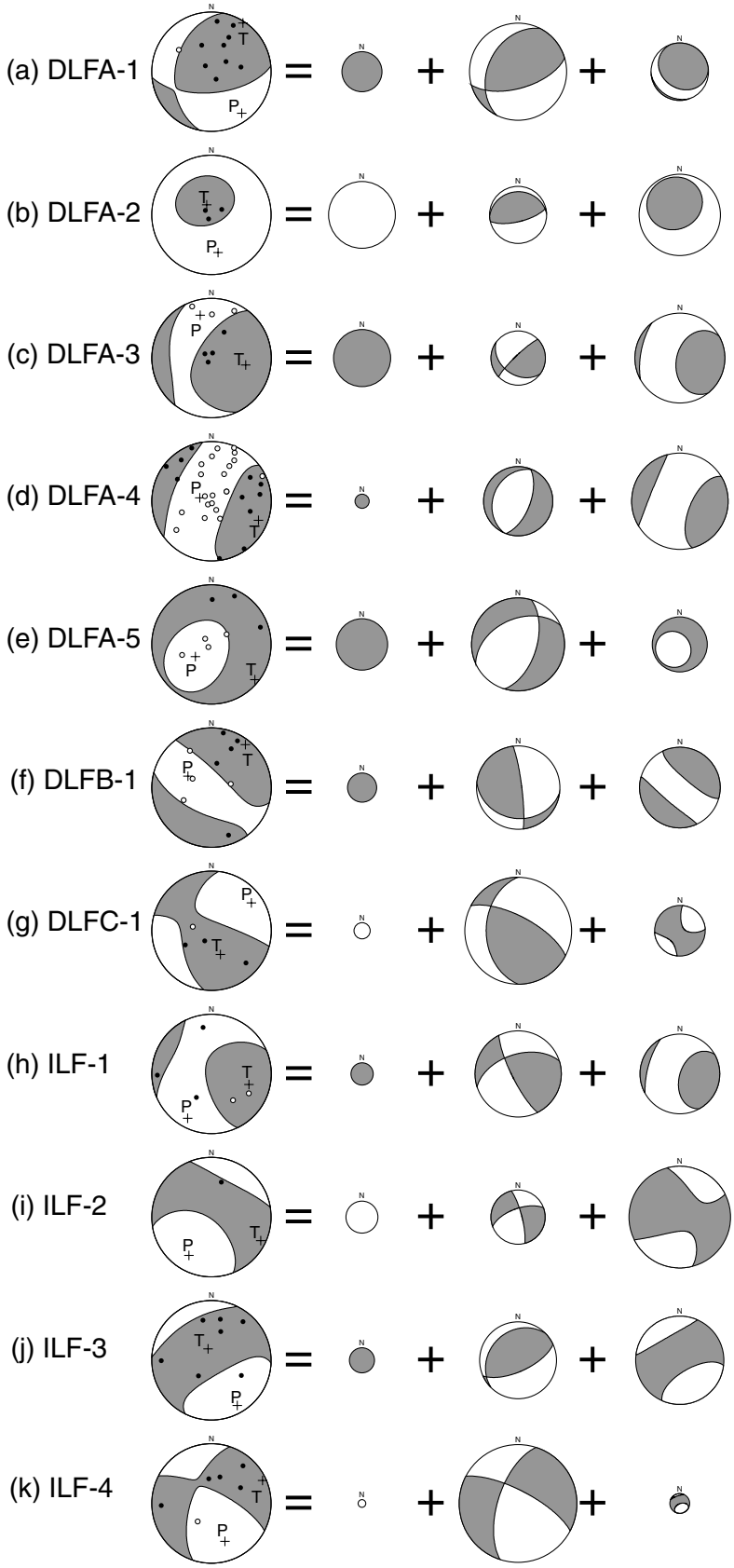

Figure 7. Source mechanisms estimated for seven DLFs and four ILFs (left). Decompositions into volumetric, DC and CLVD parts of their moment tensors (right). The area of each plot is proportional to the largest principal moment. Lower focal hemispheres are shown in equal-area projection, with compressional fields shaded. The location of *P* and *T* axes are indicated with crosses. (a) DLFA-1. (b) DLFA-2. (c) DLFA-3. (d) DLFA-4. (e) DLFA-5. (f) DLFB-1. (g) DLFC-1. (h) ILF-1. (i) ILF-2. (j) ILF-3. (k) ILF-4. Most of the *P* polarities are consistent with the best source mechanisms.

Table 3. Percentage of volumetric, double-couple and CLVD components, residuals and AIC values for moment tensor solutions and single-force solutions of intermediate-depth low-frequency events.

Event ID	Moment tensor component (per cent)			Residual		AIC	
	Volumetric	DC	CLVD	MT	SF	MT	SF
DLFA-1	11	66	23	0.3397	0.3635	1985	2055
DLFA-2	31	23	46	0.4179	0.4897	1427	1535
DLFA-3	23	21	56	0.2800	0.3853	2115	2538
DLFA-4	1	34	65	0.2940	0.3255	1319	1396
DLFA-5	18	61	21	0.3818	0.3993	2240	2287
DLFB-1	6	49	45	0.1743	0.2592	326	435
DLFC-1	2	80	18	0.4532	0.4791	1363	1393
ILF-1	3	52	45	0.1407	0.2476	233	369
ILF-2	7	21	72	0.2764	0.3247	599	654
ILF-3	4	41	55	0.3325	0.3666	887	931
ILF-4	0	97	3	0.4220	0.5067	1055	1145

MT, moment tensor inversion; SF, single-force inversion.

constants, and the strongest (first) dipole is oriented in a direction normal to the crack (Aki & Richards 2002). If the total volume is conserved in the magma injection process, the three dipoles above must be accompanied by another force system with an implosive component that exactly cancels out its explosive component. If this force system is symmetrical around the crack, the resulting force system is a pure CLVD. Such cases are shown in Chouet (1996). Realistically, the compensation would not be completely symmetric. In this case the resulting force system is not expressed as pure CLVD but as a combination of DC, CLVD and volumetric components.

We present an example of source models having CLVD and DC for DLFs and ILFs. We suppose that a tensile crack is coupled with a spherical chamber. The diagonal moment components for a tensile crack that opens are represented by $\mathbf{M}_{\mathrm{C}} = (M_{xx}, M_{yy}, M_{zz}) = (1, 3, 1)$, and the diagonal components for a spherical chamber that shrinks uniformly are expressed as $\mathbf{M}_{\mathrm{S}} = (-\frac{5}{3}, -\frac{5}{3}, -\frac{5}{3})$ when $\lambda = \mu$ and non-diagonal components are zero. When the crack opens and the chamber shrinks simultaneously, the total moment tensor becomes $\mathbf{M}_{\mathrm{T}} = \frac{2}{3}(-1, 2, -1)$, which is a CLVD. If the shape of the chamber is an oblate spheroid and the chamber has an additional small moment tensor $\mathbf{M}_{\mathrm{A}} = (-0.3, 0.3, 0)$, the total moment tensor is expressed by a combination of CLVD (82 per cent) and DC (18 per cent). When $\mathbf{M}_{\mathrm{A}} = (0, 0.3, 0.3)$, the total moment tensor consists of CLVD (70 per cent), DC (18 per cent) and volumetric (12 per cent). Therefore, we conclude that a combination source consisting of a tensile crack and oblate spheroid magma chamber can explain the observed moment tensor components of DLFs and ILFs. In this source model, an LF earthquake is generated when magma suddenly moves from a crack to a chamber or vice versa. The orientations of the principal axes of the moment tensors of DLFs and ILFs suggest that complex magma movements within the concentrated focal regions cause the DLFs and ILFs.

Although we do not adopt the source mechanisms including single-force components, the force components are important for characterizing the friction force associated with magmatic fluid flow (Ukawa & Ohtake 1987) and releasing gravitational energy accumulated by the density contrast between the solid and the melt (Takei & Kumazawa 1994).

The high-frequency waves at the onset of *P* and *S* waves on DLFA-2 (Fig. 2a) are interpreted to being generated by the breaking of a barrier between the crack and the chamber when magma starts moving. The vibration of tensile cracks effectively produces both the volumetric components in the source mechanisms and the long coda waves. Therefore, the vibration of tensile cracks would explain the significant volumetric component (31 per cent) of the source mechanism of DLFA-2, which has 1 Hz coda waves lasting roughly 20 s or more (Fig. 2a). The width of the spectral peaks is related to the Q of the vibrator, which is shown to be nearly proportional to the impedance contrast between the solid and the fluid. Aki *et al.* (1977) showed that the damping of vibrations of the fundamental mode of a liquid body is determined by the impedance contrast between the solid and the fluid. They obtained the formula

$$Q = \frac{\pi}{\ln[(Z+1)/(Z-1)]}, \tag{6}$$

where Z is the impedance contrast: $Z = \rho_{\mathrm{s}}\alpha/\rho_{\mathrm{f}}v$; ρ_{s} and ρ_{f} are the densities of the solid and fluid, respectively. α is the P wave velocity, v is the acoustic wave velocity in magma. Here, we adopt $\rho_{\mathrm{f}} = 2.7$ g cm^{-3} and $v = 2.2$ km s^{-1}, which are appropriate for basaltic magma (Murase & McBirney 1973). $\rho_{\mathrm{s}} = 3.0$ g cm^{-3} and $\alpha = 7.8$ km s^{-1} are also adopted following the structure at a depth of 33 km in Tanaka *et al.* (2002). Then, we obtain $Z \simeq 4.0$ and $Q \simeq 6.2$ from eq. (6). The Q value for the fundamental mode is obtained from observed spectra using the standard relation $Q = f/\Delta f$, where f is the frequency of the spectral peak and Δf is the width of the peak at its half-energy level (Aki & Richards 2002). The Q value of the S wave, of which the peak frequency is 1 Hz, is measured at each station, and then we obtain an average value of $Q = 6.0 \pm 0.3$ ($f = 1.0$, $\Delta f = 0.167 \pm 0.08$). Thus, the observed Q value is close to the predicted value of $Q \simeq 6.2$. Therefore, it is plausible for the source mechanism for 1 Hz waves of DLFA-2 to be interpreted as the vibration of a basaltic-magma-filled crack.

As mentioned previously, the source mechanisms of DLFs and ILFs have DC and CLVD components and those of some DLFs also have a significant volumetric component. Although a scalar seismic moment for LF is required to account for a volume change at the source of LF, we have not obtained the scalar seismic moments by the spectral ratio method. Here, we estimate the volume change at the source for the event DLFA-2 for which the local magnitude is 1.4. The scalar seismic moment of this event is approximately 1.3×10^{11} N m. We consider only a volumetric (isotropic) component for estimating a volume change at the source of LF, since CLVD sources produce no volume change. The scalar moment of the volumetric component is approximately 4.1×10^{10} N m, which is 31 per cent of the total scalar seismic moment. For $\lambda = \mu = 1.7 \times 10^{10}$ Pa, the two volume-change values $\Delta V_{\mathrm{cr}} = M_{\mathrm{vol}}/(\lambda + 2\mu/3) = 1.45$ m^3 and $\Delta V_{\mathrm{sph}} = M_{\mathrm{vol}}/(\lambda + 2\mu) = 0.80$ m^3 are obtained for a crack and a general explosion or implosion, respectively (Müller 2001). The

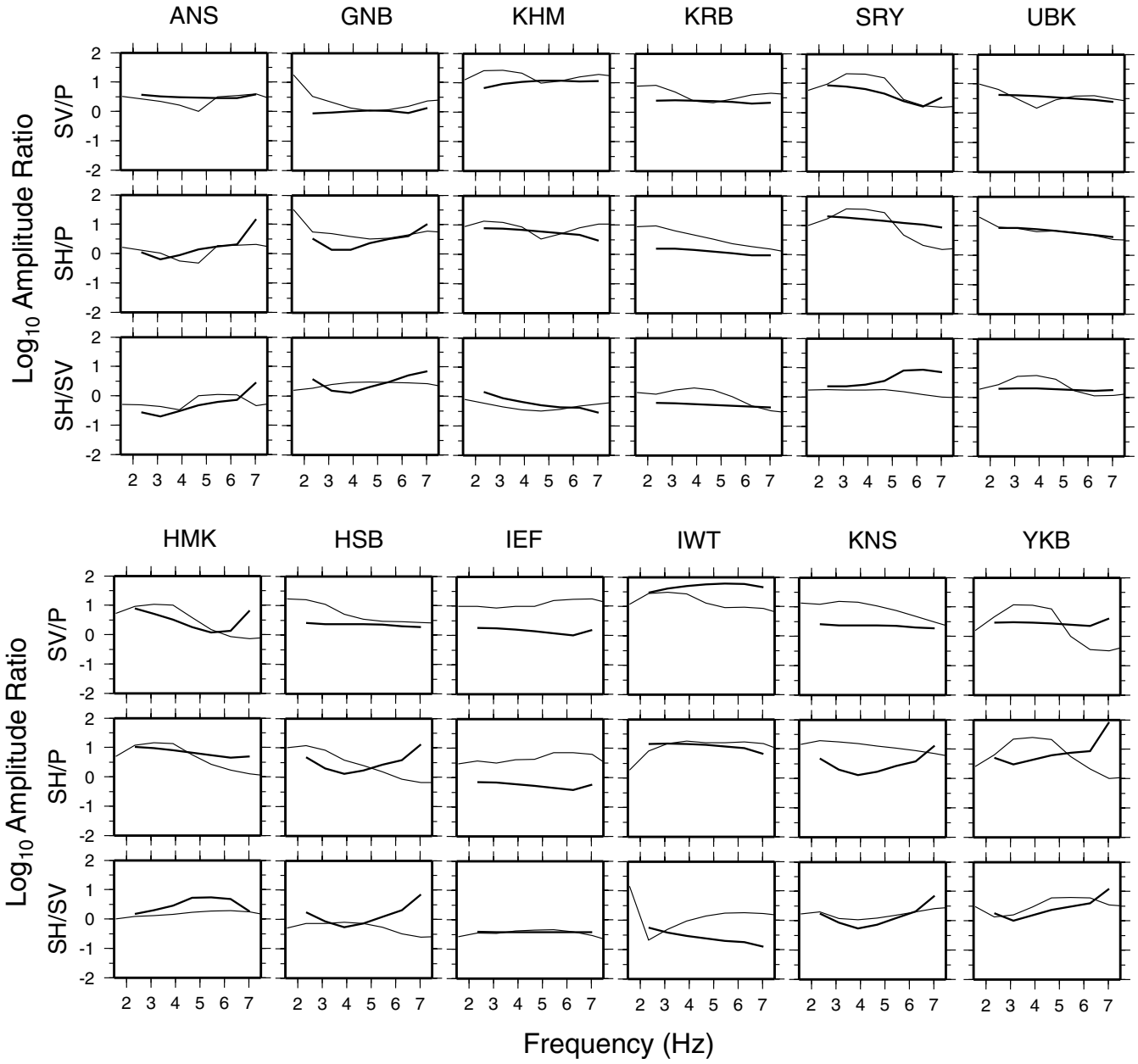

Figure 8. Comparisons of the observed amplitude spectral ratios (thin lines) and the theoretical amplitude spectral ratios (thick lines) for the best-fitting moment tensor models for ILF-3. The theoretical amplitude ratios fit those observed fairly well.

former probably gives an upper limit for the true volume change ΔV, causing $\mathbf{M}_{\mathrm{vol}}$, whereas the latter may represent a lower limit (Müller 2001).

6.3 Activity of deep and intermediate-depth low-frequency earthquakes

In 1995 September, the first significant volcanic tremor and ILFs were observed at a depth of 8 km beneath Iwate volcano (Ueki *et al.* 1996). Hence, to examine the temporal change in the seismic activity from 1995 September, we relocate the hypocentres of DLFs and ILFs only from the data of the permanent stations that operated at that time. To reduce the errors in the hypocentral locations, we first calculate the station corrections for the stations installed before 1998. We use the residuals of the arrival times for the DLFs and ILFs located by the JHD method in the previous section.

We plot focal depths of ILFs in the period from 1995 September to 2000 June in Fig. 10(a). We find that remarkable temporal changes occur in focal depth from 1998 April to 2000 June. The hypocentres were mainly distributed in the depth range 7–10 km from 1995 September to 1998 April, whereas the hypocentral range expanded to 5–12 km depth from 1998 April to October. Most of the ILFs occurred at depths of 8–12 km until 1999 September; then the depth range changed again to 6–11 km. As suggested for the cases of vertical migration of seismicity at Mt St Helens and Mt Spurr (Shemeta & Weaver 1986; Power *et al.* 1995), here the migrations are considered to be a manifestation of recharge and migration of magma and/or readjustments of stress to magma movement around the hypocentral region.

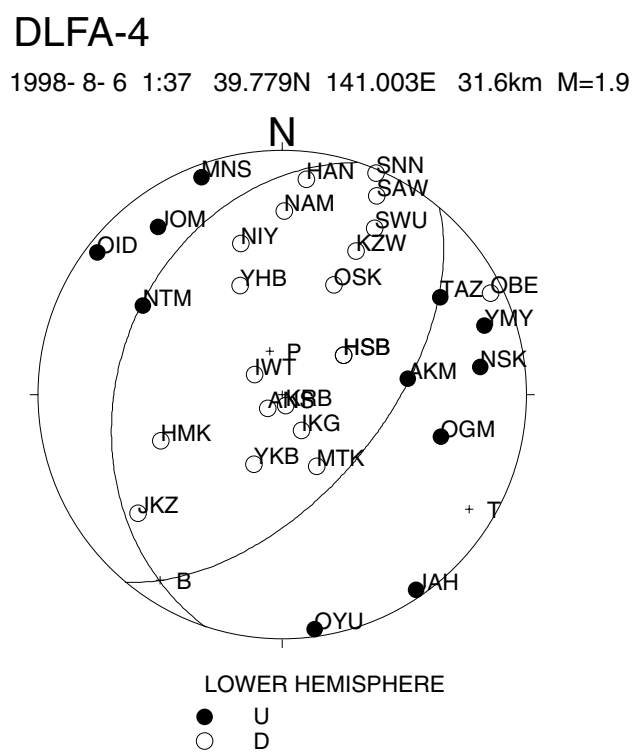

Figure 9. A normal-fault mechanism and distribution of *P*-wave first-motion polarities for DLFA-4. Compressional and dilatational first motions of *P* waves are shown by solid and open circles, respectively, and are plotted on the lower focal hemisphere in equal-area projection.

Fig. 10(b) shows the spatial and temporal variation of DLFs in a depth–time plot. We do not find significant changes in the focal depth distribution for DLFs of groups A and B between 1995 September and 2000 June. DLF group C is several kilometres deeper, and occurred only from 1999 March 15–20.

The shallow seismic activity of Iwate volcano during 1998–1999 was associated with crustal deformation (Tanaka *et al.* 2002). We evaluate shallow seismic activity by plotting the cumulative number of SHFs from the beginning of activity in 1998. We compare the cumulative numbers of DLFs and ILFs in 1998–1999 with those of SHFs in Fig. 11. The activity of the DLFs and ILFs became very high, and it is recognized that their temporal evolution is well correlated with that of the SHFs. The numbers of SHFs and DLFs increased significantly in the period from 1998 April to August and continued to increase at a lower rate during late 1998 and 1999. An $M = 6.1$ earthquake occurred on 1998 September 3 at approximately 10 km southwest of the summit of the volcano (Umino *et al.* 1998; Nakahara *et al.* 2002), but this earthquake had no obvious effects on the occurrence rates of DLFs and ILFs (Fig. 11a). Even after removal of the aftershocks (Tanaka *et al.* 1999) from the tabulation, one can still see an increase in the rate of shallow volcanic earthquakes at this time.

To examine the onset of those activities closely, we enlarge the time axis and plot the numbers of SHFs and DLFs in the period from 1998 March to May. It is noteworthy that the onset of the abrupt increase of DLF earthquakes on 1998 April 24 was followed 5 days later by that of SHF earthquakes on 1998 April 29 (Fig. 11b). This suggests that there is a causal relationship between SHF and DLF seismicity, because such temporal correlations between DLFs and volcanic eruptions have been reported for several active volcanoes. For example, during the 1991 catastrophic eruption of Pinatubo volcano, Philippines, the largest eruption in the 20th century, a striking temporal correlation between DLF activity and geological and seismological changes at the surface was observed (White 1996). At Mount Spurr, Alaska, DLF activity began to increase 4 months before the 1992 eruptions and peaked after the eruptions (Power *et al.* 1995). Four DLF earthquakes beneath Miyake Island, Japan were observed in the period from 1999 January to 2000 April before the 2000 eruption (Fujita & Ukawa 2000). Although the activity of Iwate volcano has gradually decreased and no eruption has been reported as of 2003 June, the temporal correlation of DLFs and shallow activity is probably a representation of physical connections between the deep and shallow regions. However, our analyses show that no systematic features are found in the source mechanisms of DLFs. These results suggest that the magmatic system connecting the deep region (that is the source region of DLFs) to the shallow part of the volcano is not simple and a complex magma plumbing system has been activated in both deep and shallow crust during the volcanic unrest of Iwate volcano.

7 CONCLUSIONS

We have determined the hypocentre distributions and source mechanisms of the DLFs and ILFs by analysing data from a dense seismic network in and around Iwate volcano. The main results are summarized as follows: (1) DLFs are located within three concentrated regions: the first group is located at 32 km depth, approximately 10 km south of the summit, the second is at 33 km depth, approximately 10 km northeast of the summit and the third is at 37 km depth approximately 7 km northeast of the summit. ILFs are located within a nearly vertical pipe-like region extending in depth from 5 to 12 km beneath the volcano. (2) Source mechanisms of DLFs and ILFs consist of CLVD and DC components. Some DLFs show a significant volumetric component in their source mechanism. (3) Opening of a tensile crack coupled with a shear crack or with the volume change of an oblate spheroid magma chamber can generate DLFs and ILFs of volumetric, CLVD and DC mechanisms. (4) No characteristic orientations of the principal axes of the moment tensors of DLFs and ILFs are recognized. The above results suggest the existence of a complex magma system at the concentrated focal regions of DLFs and ILFs.

ACKNOWLEDGMENTS

The first author (HN) is indebted to T. Hirasawa, M. Ohtake, H. Sato and H. Fujimoto for their valuable advice during this study. We also thank all the members of the Research Center for Prediction of Earthquakes and Volcanic Eruptions, Graduate School of Science, Tohoku University, for their stimulating discussions and their kind cooperation in our seismic observations. We are grateful to those who participated in the 1997–1999 Joint Seismic Observation. We also thank the staff of JMA for allowing us to use the data of JMA. We are grateful to T. Wright, G.R. Foulger and an anonymous reviewer for reviewing our manuscript and their valuable comments. We used D. Carroll's genetic algorithm driver (Carroll 2001) and would like to thank him. Almost all figures were produced with GMT (Wessel & Smith 1998). The field work was partly supported by a special grant in 1998 from the Ministry of Education and Culture and by Grant-in Aid for Scientific Research (C) (2) 09640499 to SU.

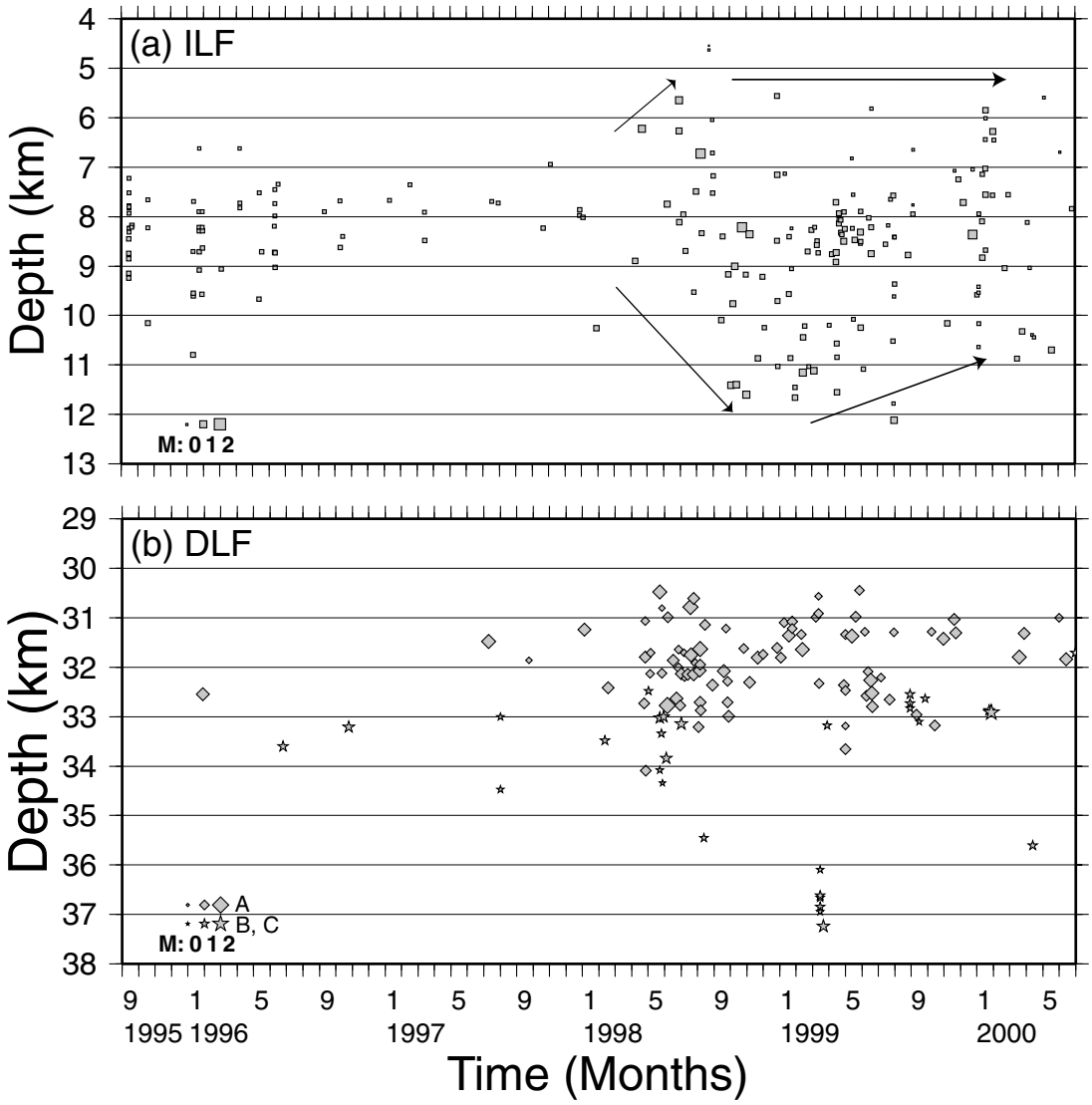

Figure 10. Depth–time diagram of (a) ILFs and (b) DLFs in the period from 1995 September to 2000 June. The grey squares and diamonds show the depths of ILFs and the south DLFs (group A), respectively. The grey stars show the depths of the northeast DLFs (groups B and C).

REFERENCES

Akaike, H., 1973. Information theory and an extension of the maximum likelihood principle, *2nd Int. Symp. on Information Theory,* pp. 267–281, eds Petrov, B.N. & Casaki, F., Akademinai Kiado, Budapest.

Aki, K., 1984. Evidence for magma intrusion during the Mammoth Lakes earthquakes of May 1980 and implications of the absence of volcanic (harmonic) tremor, *J. geophys. Res.,* **89,** 7689–7696.

Aki, K. & Richards, P.G., 2002. *Quantitative Seismology,* 2nd edn, Univ. Science Books, Sausalito, CA.

Aki, K., Fehler, M. & Das, S., 1977. Source mechanism of volcanic tremor: fluid-driven crack models and their application to the 1963 Kilauea eruption, *J. volc. geotherm. Res.,* **2,** 259–287.

Bouchon, M., 1979. Discrete wave-number representation of elastic wave fields in three-space dimensions, *J. geophys. Res.,* **84,** 3609–3614.

Bouchon, M., 1981. A simple method to calculate Green's functions for elastic layered media, *Bull. seism. Soc. Am.,* **71,** 959–971.

Carroll, D.L., 2001. FORTRAN Genetic Algorithm Driver (http://cuaerospace.com/carroll/ga.html).

Chouet, B.A., 1996. New methods and future trends in seismological volcano monitoring, in *Monitoring and Mitigation of Volcano Hazards,* pp. 23–97, eds Scarpa, R. & Tilling, R.I., Springer-Verlag, Berlin.

Crosson, R.S. & Bame, D.A., 1985. A spherical source model for low-frequency volcanic earthquakes, *J. geophys. Res.,* **90,** 10 237–10 247.

Dahlen, F.A. & Tromp, J., 1998. *Theoretical Global Seismology,* Princeton University Press, Princeton.

Douglas, A., 1967. Joint epicentre determination, *Nature,* **215,** 47–48.

Fujita, E. & Ukawa, M., 2000. Deep low-frequency earthquakes beneath Miyakejima volcano (in Japanese with English abstract), *Bull. volc. Soc. Jpn,* **45,** 295–299.

Goldberg, D.E., 1989. *Genetic Algorithms in Search, Optimization, and Machine Learning,* Addison-Wesley, Reading.

Hasegawa, A. & Hirata, N., 1999. Summary: transect of the northeastern Japan arc—arc deformation and crustal activity, *Chikyu Monthly,* **27,** 5–11 (in Japanese).

Hasegawa, A. & Yamamoto, A., 1994. Deep, low-frequency microearthquakes in or around seismic low-velocity zones beneath active volcanoes in northeastern Japan, *Tectonophysics,* **233,** 233–252.

Hasegawa, A., Zhao, D., Hori, S., Yamamoto, A. & Horiuchi, S., 1991. Deep structure of the northeastern Japan arc and its relationship to seismic and volcanic activity, *Nature,* **352,** 683–689.

Hill, D.P., 1977. A model for earthquake swarms, *J. geophys. Res.,* **82,** 1347–1352.

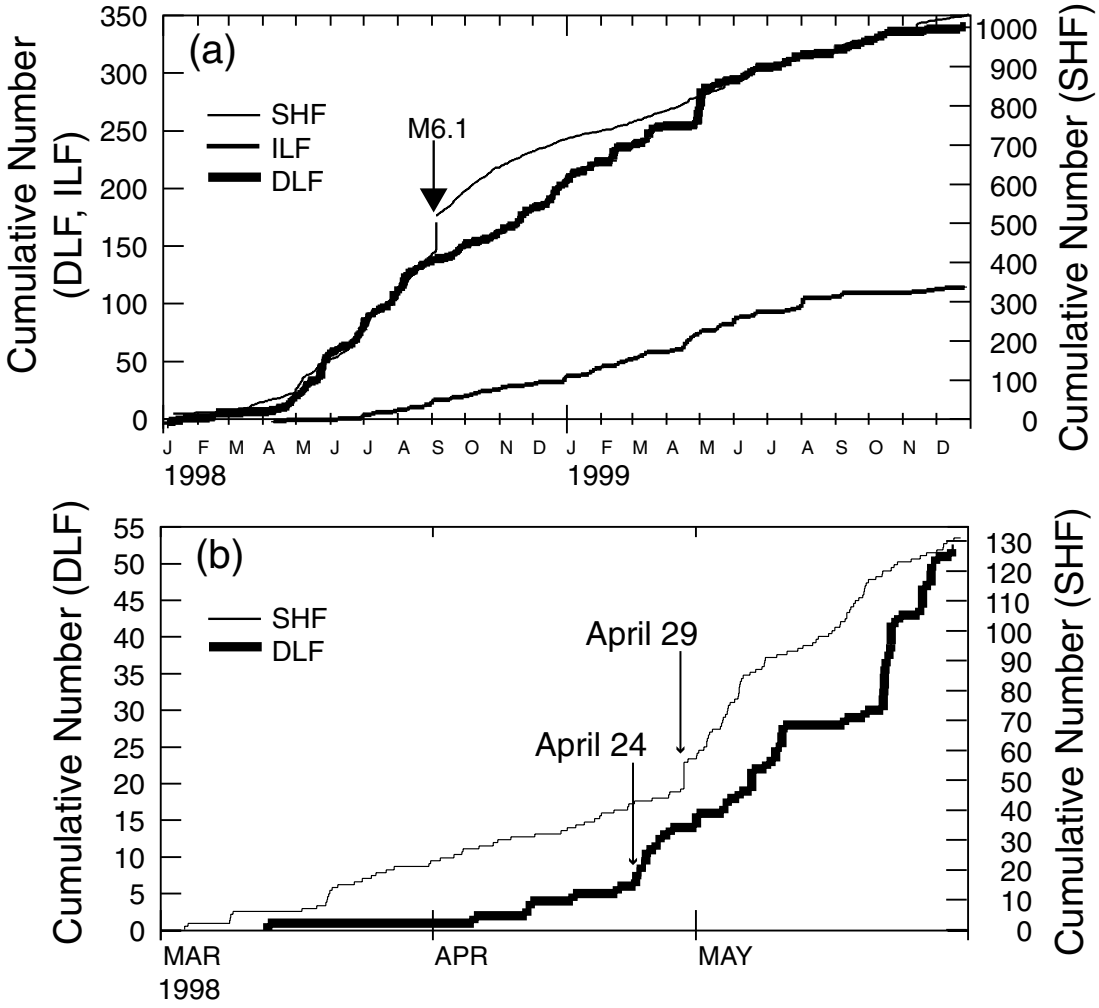

Figure 11. (a) Cumulative frequencies of SHFs, ILFs and DLFs plotted against time during 1998 and 1999. Thin, thick and very thick lines show the cumulative numbers of SHFs, ILFs and DLFs, respectively. An arrow indicates the $M = 6.1$ earthquake of 1998 September 3. The SHFs are located in the region bounded by the latitudes of 39.8°N and 39.9°N and longitudes of 140.85°E and 141.10°E. (b) Cumulative frequencies of SHFs and DLFs plotted versus time from 1998 March to May. Arrows indicate the onsets of the abrupt increases of SHFs.

Holland, J.H., 1975. *Adaptation in Natural and Artificial Systems,* University of Michigan Press, Ann Arbor.

Julian, B.R., 1983. Evidence for dyke intrusion earthquake mechanisms near Long Valley caldera, California, *Nature,* **303,** 323–325.

Julian, B.R. & Foulger, G.R., 1996. Earthquake mechanisms from linear–programming inversion of seismic-wave amplitude ratios, *Bull. seism. Soc. Am.,* **86,** 972–980.

Julian, B.R. & Sipkin, S.A., 1985. Earthquake process in the Long Valley Caldera area, California, *J. geophys. Res.,* **90,** 11 155–11 169.

Julian, B.R., Miller, A.D. & Foulger, G.R., 1998. Non-double-couple earthquakes, 1: theory, *Rev. Geophys.,* **36,** 525–549.

Kanamori, H., Eksröm, G., Dziewonski, A., Baker, J.S. & Sipkin, S.A., 1993. Seismic radiation by magma injection: an anomalous seismic event near Tori Shima, Japan, *J. geophys. Res.,* **98,** 6511–6522.

Kennett, B.L.N. & Kerry, N.J., 1979. Seismic waves in a stratified half-space, *Geophys. J. R. astr. Soc.,* **57,** 557–583.

Knopoff, L. & Randall, M.J., 1970. The compensated linear-vector dipole: a possible mechanism for deep earthquakes, *J. geophys. Res.,* **75,** 4957–4963.

Koyanagi, R.Y., Chouet, B. & Aki, K., 1987. Origin of volcanic tremor in Hawaii Part I. Data from the Hawaiian Volcano Observatory 1969–1985, in *Volcanism in Hawaii,* Vol. 2, pp. 1221–1257, eds Decker, R.W. Wright, T.W. & Stauffer, P.H., US Geol. Surv. prof. Paper, 1350.

McNutt, S.R., 1994. Volcanic tremor from around the world: 1992 update, *Acta Vulc.,* **5,** 197–200.

Miller, A.D., Foulger, G.R. & Julian, B.R., 1998. Non-double-couple earthquakes, 2: observations, *Rev. Geophys.,* **36,** 551–568.

Miura, S., Ueki, S., Sato, T., Tachibana, K. & Hamaguchi, H., 2000. Crustal deformation associated with the 1998 seismo-volcanic crisis of Iwate Volcano, northeastern Japan, as observed by a dense GPS network, *Earth planets and Space,* **52,** 1003–1008.

Müller, G., 2001. Volume change of seismic sources from moment tensors, *Bull. seism. Soc. Am.,* **91,** 880–884

Murase, T. & McBirney, A.R., 1973. Properties of some common igneous rocks and their melts at high temperatures, *Geol. Soc. Am. Bull.,* **84,** 3563–3592.

Nakahara, H., Nishimura, T., Sato, H., Ohtake, M., Kinoshita, S. & Hamaguchi, H., 2002. Broad-band source process of the 1998 Iwate Prefecture, Japan, earthquake as revealed from inversion analyses of seismic waveforms and envelopes, *Bull. seism. Soc. Am.,* **92,** 1708–1720.

Nakajima, J., Matsuzawa, T., Hasegawa, A. & Zhao, D., 2001. Seismic imaging of arc magma and fluids under the central part of northeastern Japan, *Tectonophysics,* **341,** 1–17.

Nakamichi, H., 2000. Deep magmatic activity inferred from low-frequency earthquakes and fine *S* wave velocity structure beneath Iwate volcano, Japan, *PhD thesis,* Tohoku University, Sendai.

Natale, G.D., Zollo, Ferraro, A. & Virieux, J., 1995. Accurate fault mechanism determinations for a 1984 earthquake swarm at Campi Flegrei caldera (Italy) during an unrest episode: implications for volcanological research, *J. geophys. Res.,* **100,** 24 167–24 185.

Nishidomi, I. & Takeo, M., 1996. Seismicity and a focal mechanism of low-frequency earthquakes occurring in the western part of Tochigi prefecture, Japan (in Japanese with English abstract), *Bull. volc. Soc. Jpn,* **41,** 43–59.

Nishimura, T., Hamaguchi, H. & Ueki, S., 1995. Source mechanism of volcanic tremor and low-frequency earthquakes associated with the 1988–1989 eruptive activity of Mt Tokachi, Hokkaido, Japan, *Geophys. J. Int.,* **121,** 444–458.

Nishimura, T. *et al.*, 2000. Source process of very long period seismic events associated with the 1998 activity of Iwate Volcano, northeastern Japan, *J. geophys. Res.,* **105,** 19 135–19 147.

Okada, T. & Hasegawa, A., 2000. Activity of deep low-frequency microearthquakes and their moment tensors in northeastern Japan (in Japanese with English abstract), *Bull. volc. Soc. Jpn,* **45,** 47–63.

Pitt, A.M. & Hill, D.P., 1994. Long-period earthquakes in the Long Valley Caldera region, eastern California, *Geophys. Res. Lett.,* **21,** 1679–1682.

Power, J.A., Jolly, A.D., Page, R.A. & McNutt, S.R., 1995. Seismicity and Forecasting of the 1992 eruptions of Crater Peak vent, Mount Spurr volcano, Alaska: an overview, *US Geol. Surv. Bull.,* **2139,** 149–159.

Pujol, J., 1988. Comments on the joint determination of hypocenters and station corrections, *Bull. seism. Soc. Am.,* **78,** 1179–1189.

Sakamoto, Y., Ishiguro, M. & Kitagawa, G., 1986. *Akaike Information Criterion Statics,* Riedel, Hingham.

Sambridge, M. & Drijkoningen, G., 1992. Genetic algorithms in seismic waveform inversion, *Geophys. J. Int.,* **109,** 323–342.

Sambridge, M. & Gallagher, K., 1993. Earthquake hypocenter location using genetic algorithms, *Bull. seism. Soc. Am.,* **83,** 1467–1491.

Sato, M. & Hamaguchi, H., 1999. Analysis of crustal deformation of Mount Iwate observed for a period from February to August 1998, *Chikyu Monthly,* **21,** 312–317 (in Japanese).

Sen, M.K. & Stoffa, P.L., 1992. Rapid sampling of model space using genetic algorithms: examples from seismic waveform inversion, *Geophys. J. Int.,* **108,** 281–292.

Shaw, H.R., 1980. The fracture mechanisms of magma transport from the mantle to the surface, in *Physics of Magmatic Processes,* pp. 201–264, ed. Hargraves, R.B., Princeton University Press, Princeton.

Shemeta, J.E. & Weaver, C.S., 1986. Seismicity accompanying the May 18, 1980 eruption of Mount St Helens, Washington, in *Mount St Helens: Five Years Later,* pp. 44–58, ed. Keller, S.A.C., Eastern Washington University Press, Washington.

Shimizu, H., Ueki, S. & Koyama, J., 1987. A tensile–shear crack model for the mechanism of volcanic earthquakes, *Tectonophysics,* **144,** 287–300.

Soosalu, H. & Einarsson, P., 1997. Seismicity around the Hekla and Torfajökull volcanoes, Iceland, during a volcanically quiet period, 1991–1995, *Bull. Volc.,* **59,** 36–48.

Takei, Y. & Kumazawa, M., 1994. Why have the single force and torque been excluded from seismic source models?, *Geophys. J. Int.,* **118,** 20–30.

Tanaka, S., Nakamichi, H., Hamaguchi, H. & Ueki, S., 1999. The 1998 seismic activity of Mount Iwate, *Chikyu Monthly,* **21,** 273–279 (in Japanese).

Tanaka, S., Hamaguchi, H., Ueki, S., Sato, M. & Nakamichi, H., 2002. Migration of seismic activity during the 1998 volcanic unrest at Iwate volcano, northeastern Japan, with reference to *P* and *S* wave velocity anomaly and crustal deformation, *J. volc. geotherm. Res.,* **113,** 399–414.

Tsumura, N., Matsumoto, S., Horiuchi, S. & Hasegawa, A., 2000. Three-dimensional attenuation structure beneath the northeastern Japan arc estimated from spectra of small earthquakes, *Tectonophysics,* **319,** 241–260.

Ueki, S., Morita, Y. & Hamaguchi, H., 1996. On the volcanic tremor observed at Mount Iwate in September and October, 1995, *Tohoku J. natural Disaster Sci.,* **32,** 285–292 (in Japanese).

Ueki, S., Miura, S., Sato, T., Tachibana, K. & Hamaguchi, H., 1999. The 1998 activity of crustal deformation of Mount Iwate detected by a dense GPS network observation, *Chikyu Monthly,* **21,** 296–302 (in Japanese).

Ukawa, M. & Ohtake, M., 1987. A monochromatic earthquake suggesting deep-seated magmatic activity beneath the Izu-Ooshima volcano, Japan, *J. geophys. Res.,* **92,** 12 649–12 663.

Umino, N. *et al.*, 1998. Aftershock distribution for the $M = 6.1$ earthquakes of 3 September 1998 in Shizukuishi, Iwate Prefecture, northeastern Japan, *Active Fault Research,* **17,** 1–8(in Japanese).

Urabe, T., Hirata, N. & Takano, K., 1998. A nation-wide seismic telemetry network in Japan using satellite communication, *EOS, Trans. Am. geophys. Un.,* **79**, F569.

Wessel, P. & Smith, W.H., 1998. New, improved version of Generic Mapping Tools released, *EOS, Trans. Am. geophys. Un.,* **79,** 579.

White, R.A., 1996. Precursory deep long-period earthquakes at Mount Pinatubo: spatio-temporal link to a basalt trigger, in *Fire and Mud Eruptions and lahars of Mount Pinatubo, Philippines,* pp. 307–327, eds Newhall, C.G. & Punongbayan, R.S., Philippine Institute of Volcanology.